Driving large magnetic Reynolds number flow in highly ionized,unmagnetized plasmas

D. B. Weisberg, E. Peterson, J. Milhone, D. Endrizzi, C. Cooper, V. Desangles, I. Khalzov, R. Siller, C. B. Forest

June 15, 2018

Physics of Plasmas

Disclaimer

Driving large magnetic Reynolds number flow in highly ionized, unmagnetized plasmas

D. B. Weisberg,[1, 2, a)] E. Peterson,[2] J. Milhone,[2] D. Endrizzi,[2] C. Cooper,[3, 2] V. Désangles,[4] I. Khalzov,[5, 2] R. Siller,[2] and C. B. Forest[2]
[1)] *Oak Ridge Associated Universities, Oak Ridge TN*
[2)] *Department of Physics, University of Wisconsin, Madison WI*
[3)] *LLNL, Livermore CA*
[4)] *Univ Lyon, Ens de Lyon, Laboratoire de Physique, F-69342, Lyon, France*
[5)] *Kurchatov Institute, Moscow, Russia*

(Dated: 6 June 2018)

Electrically-driven, unmagnetized plasma flows have been generated in the Madison plasma dynamo experiment with magnetic Reynolds numbers exceeding the predicted $Rm_{crit} = 200$ threshold for flow-driven MHD instability excitation. Plasma flow is driven using ten thermally emissive lanthanum hexaboride cathodes which generate a $\boldsymbol{J} \times \boldsymbol{B}$ torque in helium and argon plasmas. Detailed Mach probe measurements of plasma velocity for two flow topologies are presented: edge-localized drive using the multi-cusp boundary field, and volumetric drive using an axial Helmholtz field. Radial velocity profiles show that edge-driven flow is established via ion viscosity but is limited by a volumetric neutral drag force, and measurements of velocity shear compare favorably to Braginskii transport theory. Volumetric flow drive is shown to produce larger velocity shear and has the correct flow profile for studying the magnetorotational instability.

I. INTRODUCTION

MHD fluid dynamics experiments necessarily rely on some mechanism for stirring flows in a controlled manner. Techniques for flow drive range from highly localized momentum injection via mechanical pumping or propulsion to global body forcing via electromagnetic drives[1]. In addition, rotating tanks can be used to impose a boundary condition on an axisymmetric flow that then viscously couples to the rest of the fluid[2]. However, the topic of *plasma hydrodynamics* is relatively unexplored, as the regime in which plasmas are flow-dominated and yet highly conducting is a major experimental frontier. The dynamics in such a system are primarily governed by hydrodynamics, with the onset of MHD physics only in the case where small magnetic diffusivity and large Alfvén Mach flow results in the growth of a flow-driven MHD instability and the magnetization of the system.

A particularly intriguing application of stirred plasmas is the investigation of astrophysical phenomena like the dynamo effect and the magnetorotational instability (MRI). Laboratory experiments have long been seen as a valuable way to gain an empirical understanding of these flow-driven MHD instabilities. The dynamo effect[3] is the mechanism thought to be responsible for the generation of magnetic energy in planetary cores, stellar convection zones, and in the interstellar medium, while the MRI is an MHD instability that accelerates the accretion of matter in weakly-magnetized astrophysical disks[4]. Both theories are well established both analytically and in numerical simulations[5–8], but lack experimental evidence to rigorously confirm these underlying physical mechanisms. Previous experiments have used both liquid metal[9–13] and plasma[14] as the conducting fluid for achieving the large dimensionless parameters necessary for exciting these instabilities, with magnetic bucket plasma confinement devices succeeding in producing the largest magnetic Reynold number (Rm) flows to date. However, these experiments have fallen short of achieving the critical Rm required for positive instability growth rates as suggested by numerical simulations of both the dynamo[15,16] and the MRI[17]. The Madison plasma dynamo experiment (MPDX) is a new magnetic ring cusp device[18] that has been constructed with the goal of reaching and surpassing critical Rm thresholds for instability excitation .

In order to observe the dynamo or the MRI in the laboratory a plasma experiment must meet certain criteria, usually expressed in dimensionless terms. The confined plasma must have a large amount of kinetic energy stored in fluid flows but these flows cannot be initially magnetized, otherwise the Lorentz force will modify the global flow geometry and prevent instability excitation. The confined plasma must also be highly conducting so that plasma flows can easily advect magnetic field without appreciable magnetic diffusion. These conditions are expressed using the Reynolds number Re, the magnetic Reynolds number Rm, and the Alfvénic mach number Ma,

$$Re = VR/\nu = 0.52\frac{n_{18}\sqrt{\mu}\lambda Z^4 V_{km/s} R_m}{T_{i,eV}^{5/2}}, \tag{1}$$

$$Rm = \mu_0 \sigma V R = 12.2\frac{T_{e,eV}^{3/2} V_{km/s} R_m}{\lambda Z}, \tag{2}$$

$$Ma = V/V_A = 0.46\frac{\sqrt{n_{18}\mu} V_{km/s}}{B_G}, \tag{3}$$

where V and R are the characteristic velocity and

[a)] Electronic mail: dweisberg@gmail.com

TABLE I. Measured and dimensionless parameters for each stirring experiment, evaluated at timepoint of maximum *Rm*.

Flow type	T_e (eV)	T_i (eV)	$n_e \times 10^{17}$ (m^{-3})	f_{ion} (%)	V_{max} (km/s)	Rm	Re	Ma	χ
Counter-rotating	9.2	0.76	7.8	61	6.2	210	170	10	55
Co-rotating	10.0	0.7	2.5	49	5.9	215	67	14	11
MRI He	4.9	0.36	14.4	23	1.2	10.7	219	2.65	423
MRI Ar	3.5	1.29	16.5	63	0.7	4	18	1.2	17

length scales of the experiment, ν is the kinematic viscosity, and σ is the resistivity. These terms are defined above using plasma transport parameters[19], where n_{18} is the plasma density in units of $10^{18}\,\mathrm{m}^{-3}$, T_e and T_i are in electron volts, and μ is the ion species atomic weight in amu. Z and λ are the ion charge and the Coulomb logarithm, respectively. Table I shows the measured plasma parameters and global dimensionless parameters for the four types of flow experiments detailed in this article. The plasma radius of $R = 1.3\,\mathrm{m}$ ($0.8\,\mathrm{m}$ in the MRI cases), ion charge of $Z = 1$, and core magnetic field of $B = 0.2 - 2.2\,\mathrm{G}$ (depending on applied Helmholtz field) were used in these calculations. An experiment capable of exciting flow-driven MHD instabilities will be able to confine flowing plasmas with $Re \gg 1$, $Rm \gg 1$, and $Ma > 1$.

The importance of Re and Rm is evident in the dimensionless forms of the Navier-Stokes equation and the induction equation,

$$\frac{\partial \mathbf{v}}{\partial t} = \nabla^2 \mathbf{v} - Re[(\mathbf{v}\cdot\nabla)\mathbf{v} + \nabla p] - \chi \mathbf{v}, \tag{4}$$

$$\frac{\partial \mathbf{B}}{\partial t} = \nabla^2 \mathbf{B} + Rm \nabla \times (\mathbf{v} \times \mathbf{B}). \tag{5}$$

A third dimensionless parameter χ has been added to the Navier-Stokes equation, describing the loss of ion momentum via charge-exchange collisions with stationary neutrals. As cusp-confined plasmas are typically not 100% ionized, this term can have a large effect on the equilibrium velocity field $\mathbf{v}$, especially at high densities. The dimensionless neutral drag is a function of the viscosity and the ion-neutral collision time,

$$\chi = \frac{R^2}{\nu \tau_{in}} = 0.52 \frac{\sigma_{in,18} n_{18} n_{n,18} \sqrt{\mu} \lambda Z^3 V_{km/s} R_m^2}{T_{i,eV}^2}, \tag{6}$$

where $\sigma_{in,18}$ is the ion-neutral charge-exchange cross section in units of $10^{-18}\,\mathrm{m}^2$ and $n_{n,18}$ is the neutral density in units of $10^{18}\,\mathrm{m}^{-3}$.

This report details the results of four plasma flow experiments conducted on the Madison plasma dynamo experiment. Section II outlines the experimental device and the confinement and heating techniques utilized. Section III presents flow data generated by electromagnetic stirring at the plasma edge, incorporating a hydrodynamic model that uses the measured values of Re and χ to predict global viscously-driven flows. Section IV presents a second type of flow drive, using a weak axial magnetic field to drive flow through the entire plasma volume. Section V summarizes these results as the first experimental demonstration of controlled plasma hydrodynamics.

II. DESCRIPTION OF EXPERIMENT

The Madison plasma dynamo experiment (MPDX) is a large mutli-cusp magnetic confinement plasma experiment located at the University of Wisconsin-Madison[18]. A 3.0 m diameter spherical vacuum chamber is fitted with over 3000 permanent SmCo magnets bolted to the inner wall in an axisymmetric ring cusp geometry. The magnetic polarity of each of the 36 magnetic rings is oppositely oriented with respect to the two neighboring rings, resulting in a wall-localized field that drops off exponentially with decreasing spherical radius. Plasma is produced using a set of emissive lanthanum hexaboride (LaB_6) cathodes, which are inserted through vacuum ports past the cusp magnetic field and biased with respect to molybdenum anodes located on the opposite side of the device. DC power supplies provide a constant discharge bias between 200 V and 500 V, and each cathode can source up to 120 A. Total discharge heating power is also controlled via cathode temperature, which ranges between 1100° C and 1300° C.

The ring cusp magnetic field is used to confine steady-state helium and argon discharges, wherein the narrow mirror cusp loss width allows for the sustained generation of dense, warm plasmas[20]. Scanning Langmuir probe measurements show that the bulk of the plasma is homogeneous, with no gradients in electron temperature or density. The sharp gradient that defines the plasma edge is typically 10 cm wide, and plasma density drops to zero about 10 cm from the vessel wall when measured along a radial chord bisecting two magnet rings. Fig.1 shows a cross-sectional view of the cusp field geometry, electrode positions, and typical plasma radial profiles measured along probe chords.

The spherical geometry of MPDX is described using the regular r, θ, ϕ coordinate system, but a latitude/longitude coordinate system is also used to specify port locations on the vessel wall. Cathode, anode,

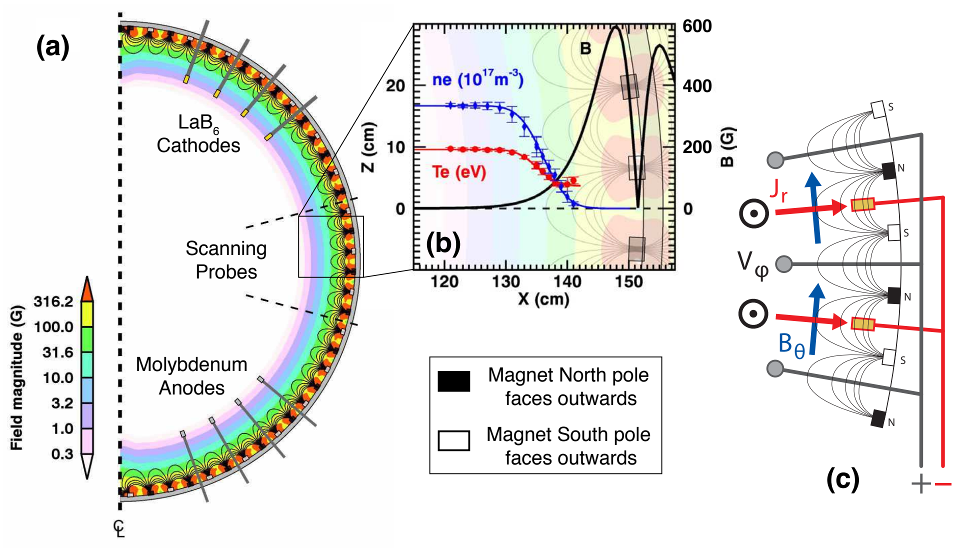

FIG. 1. Cross-sectional schematic of the MPDX vessel. a) The ring cusp magnetic field is axisymmetric about the z-axis, and electrodes and probes are inserted through ports between magnet rings. b) The cusp field decreases exponentially with radius and confines a homogeneous plasma. c) Edge toroidal flow is driven by $\boldsymbol{J} \times \boldsymbol{B}$ torque near retracted cathodes (gold), where current is sourced by inserted anodes (grey).

and scanning probe positions in this report are given using this system, where the north pole (+90, $\theta = 0$) is at the top of the poloidal cross-section in Fig.1 and the south pole (-90,$\theta = \pi$) is at the bottom. Vacuum ports are located at multiples of 5 degrees (90,85,80,...excluding the equator) with magnet rings offset by 2.5 degrees (87.5,82.5,77.5...).

The scanning probe array installed on MPDX consists of up to nine combination Langmuir/Mach probes. Each probe tip contains four planar Mach faces as well as a Langmuir wire tip, so that the local electron temperature and density is measured along with up to two components of the local ion flow Mach number. Thus each probe measures the absolute ion flow velocity in two directions: the θ (north-south) and ϕ (east-west) components of the plasma flow. In order to obtain a global picture of the plasma flow, velocity probes are distributed between the north pole and the south pole of the vacuum vessel and are scanned between the plasma edge ($r \sim 140$ cm) and their maximum insertion depth of $r = 90$ cm.

In addition to the velocity probe array, several non-invasive diagnostic systems are used to measure core plasma parameters. A mm-wave heterodyne interferometer is used to measure the line-averaged electron density, a Fabry-Perot interferometer measures core ion temperature, and a pyrometric bolometer measures radiated power at the vessel wall. Neutral pressure is measured at the vessel wall with two cold-cathode vacuum gauges, and an array of survey spectrometers measures the radial neutral density profile via optical emission spectroscopy.

III. EDGE-DRIVEN FLOW

The first method of injecting momentum into the bulk unmagnetized plasma uses the application of a $\boldsymbol{J} \times \boldsymbol{B}$ torque at the plasma's magnetized edge, as shown in Fig.1c. The emissive LaB$_6$ cathodes are retracted to a radial position closer to the vessel wall ($130 < r < 135$ cm) where the magnetic cusp field is approx. 20 G, while the molybdenum anodes are inserted well beyond the cusp field ($r \sim 115$ cm) where the uncorrected component of Earth's field is less than 0.2 G. The bulk unmagnetized plasma is thus maintained at a uniform electric potential close to the grounded anodes and all current drawn from the cathodes is directed radially. Because the cusp field is aligned in the theta direction at the cathode locations, the resulting $\boldsymbol{J} \times \boldsymbol{B}$ torque due to the discharged current is in the phi direction. This spins up the edge of the plasma in the direction determined by the polarity of the cusp field: at co-latitudes of ±85,±75,...,±15,±5 torque is in the $-\hat{\phi}$ direction, while at co-latitudes of ±80,±70,...,±20,±10 torque is in the $+\hat{\phi}$ direction.

Momentum is transported from the spinning edge into the core via ion-ion viscosity, but is lost to charge-exchange collisions with unconfined neutrals. A simple 1D form of the momentum equation is,

$$\frac{\partial v_\phi}{\partial t} = \frac{1}{mn}\left(J_r \times B_\theta\right)_\phi - \frac{v_\phi}{\tau_{in}} + \nu_{ii}\left[\nabla^2 \mathbf{v}\right], \qquad (7)$$

where the $\boldsymbol{J} \times \boldsymbol{B}$ torque is only non-zero at the plasma edge. A 2D hydrodynamic numerical code has been developed[16] to solve the axisymmetric version of this momentum transport equation, in which the toroidal velocity boundary condition at the plasma edge $v_\phi(r = R, \theta)$ is an arbitrary function of the polar angle. The transport of momentum inward is calculated using a global value of Re, where the classical unmagnetized plasma ion viscosity is calculated using measured density and ion temperature,

$$\nu = 0.96 v_{ti}^2 \tau_{ii} \propto \frac{T_i^{5/2}}{n\sqrt{\mu}}, \qquad (8)$$

where the neutral drag term is calculated using 1D neutral diffusion theory benchmarked against optical emis-

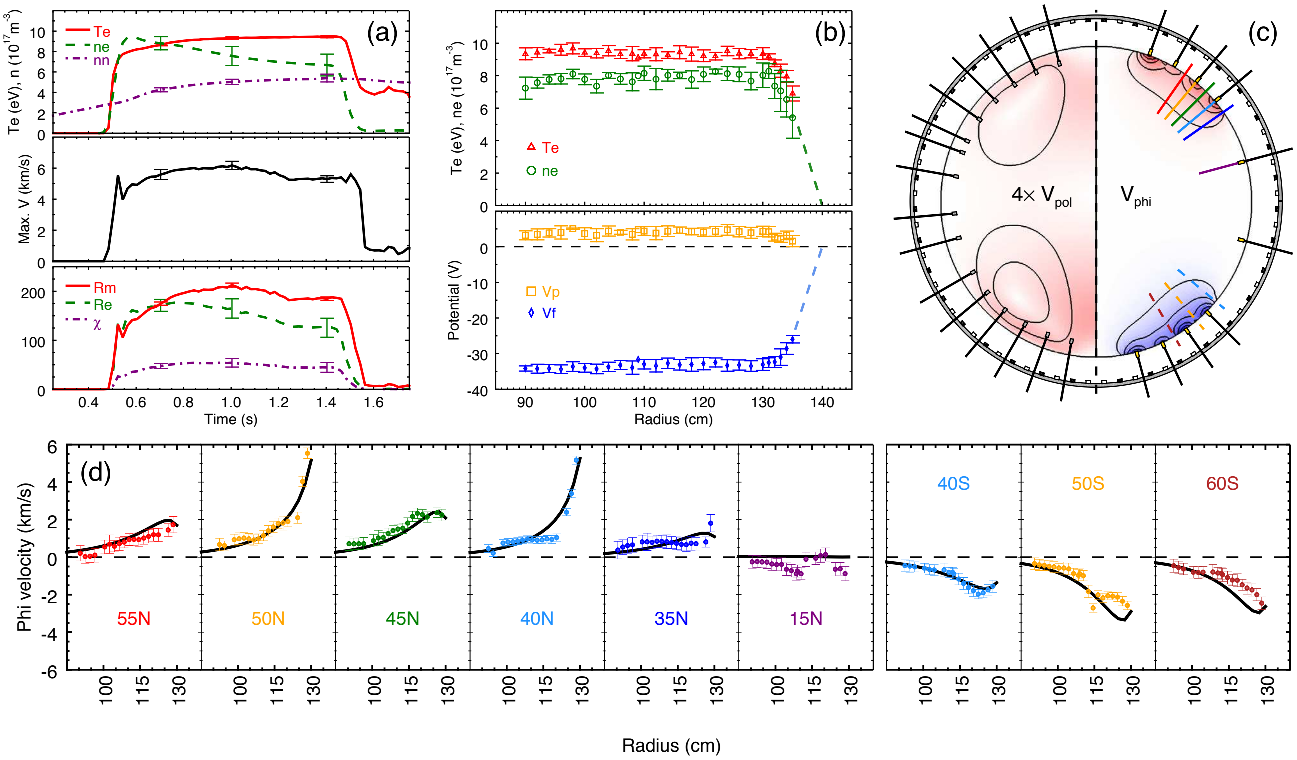

FIG. 2. Counter-rotating flow measurements in helium. a) Global plasma parameters; error bars indicate shot-to-shot variation. b) Globally averaged radial profiles from scanning Langmuir probes. c) Electrode and probe placement with modeled flow: poloidal flow contours and streamlines are shown on left, toroidal flow contours on right. d) Velocity probe radial profiles, showing counter-rotating hemispheres. Colors correspond to probe positions in (c), solid lines are modeled flow.

sion spectroscopy measurements. This transport model the predicts the neutral burn-out in the plasma core,

$$n_n(r) = A\frac{\sinh(r/\lambda_{mfp})}{r/\lambda_{mfp}}, \tag{9}$$

$$\lambda_{mfp} = v_{th,n}/(\nu_{iz} + \nu_{cx}), \tag{10}$$

$$A = \frac{n_{nR}R/\lambda_{mfp}}{\sinh(R/\lambda_{mfp})}, \tag{11}$$

where λ_{mfp} is the total neutral mean free path for ionization and charge-exchange collisions, $v_{th,n}$ is the neutral thermal velocity (based on room temperature $T_n = 0.025\,\mathrm{eV}$) and n_{nR} is the neutral density at the wall ($r = R$). Thus the amount of neutral burn-out is encoded in the radial profile of the dimensionless neutral drag χ. The details of this hydrodynamic solver are discussed further in the Appendix.

The strategic placement of cathodes allows the edge plasma flow to be arbitrarily controlled and permits the realization of a wide possibility of flow geometries. Edge flow is primarily a function of cathode latitudinal location and cathode discharge power, as well as the strength of the edge field at the cathode radial position. The two main flow geometries established using this technique are a) counter-rotating hemispheres and b) co-rotating hemispheres. These correspond to the T_1 and T_2 toroidal flow harmonics in the spherical expansions of Bullard and Gellman[21] and at lower enough viscosity both result in one poloidal circulation cell in each hemisphere. The only hardware limitation on the edge rotation profile is the presence of Helmholtz coils which block cathode installation at latitudes of 35° and 30° in both the northern and southern hemispheres. This explains the conspicuous gap in cathode placement evident in the experimental setups presented in the following sections.

A. Counter-rotating hemispheres

Resistive MDH simulations have shown that counter-rotating hemispheres in a sphere generates a laminar flow geometry that is capable of exciting the dynamo instability[16]. In a spherical analog to von-Karman flow, the oppositely directed toroidal flow in the north and south hemispheres can drive two poloidal flow cells, with strong radial outflow from the equator to the poles and a weaker inflow at the equatorial plane. This so-called 'two-vortex' flow can, at large enough Rm, advect and amplify a weak transverse seed magnetic field through a stretch-twist-fold mechanism. The transition to positive magnetic growth rates has been shown to be very sensitive to details of the flow geometry, and so well-established flow control is important in a dynamo exper-

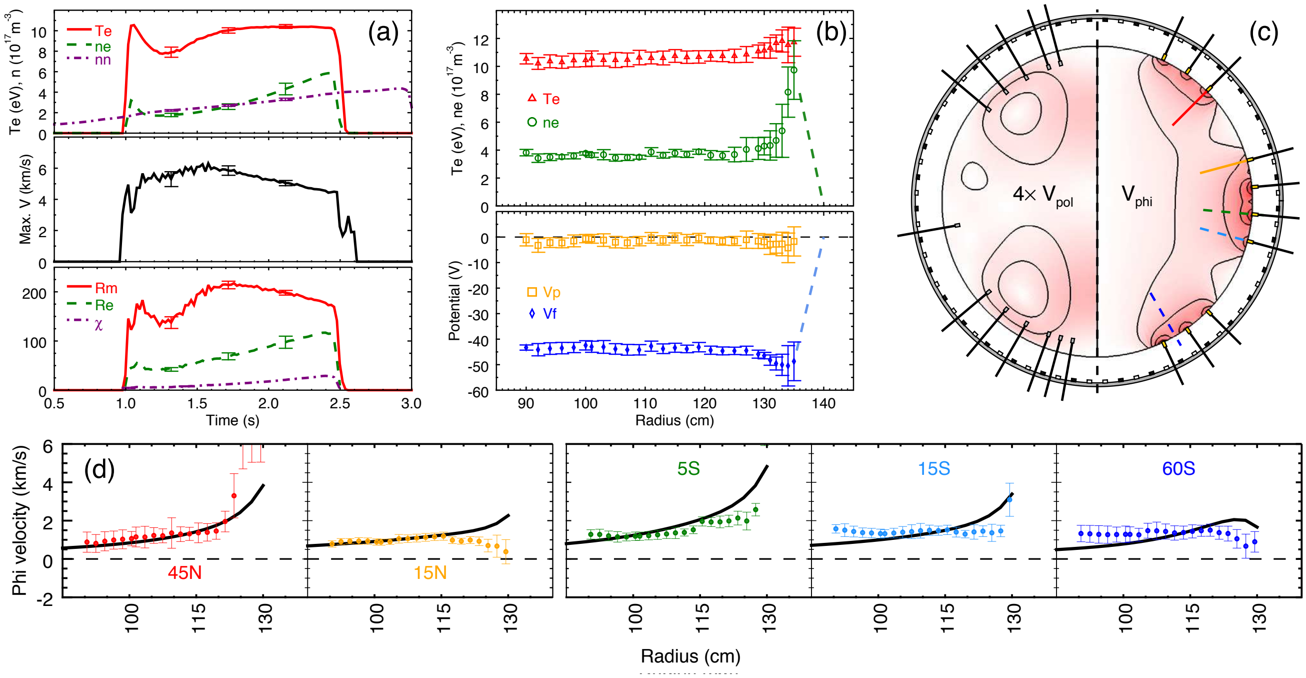

FIG. 3. Co-rotating flow measurements in helium. a) Global plasma parameters; error bars indicate shot-to-shot variation. b) Globally averaged radial profiles from scanning Langmuir probes. c) Electrode and probe placement with modeled flow: poloidal flow contours and streamlines are shown on left, toroidal flow contours on right. d) Velocity probe radial profiles, showing co-rotating hemispheres. Colors correspond to probe positions in (c), solid lines are modeled flow.

iment.

To drive counter-rotating flow in MPDX, 8 cathodes were distributed at mid-to-high latitudes in both the north and south hemispheres and were retracted into the cusp so the LaB$_6$ spanned the radial interval $130 < r < 135\,\mathrm{cm}$. Two additional cathodes near the equator were not retracted and were used only to provide additional heating power without affecting the edge flow. Nine velocity probes were scanned between $r = 90\,\mathrm{cm}$ and $r = 130\,\mathrm{cm}$, and their electron density measurements in the plasma core were calibrated to the line-averaged mm-wave interferometer measurements.

Fig.2 shows the results from the counter-rotating experiment, including the results of 2D hydrodynamic modeling. The maximum flow velocity was measured to be 6 km/s, resulting in dimensionless parameters of $Re = 170$, $Rm = 210$, and $\chi_{wall} = 55$. The results of the hydrodynamic simulations compare favorably with velocity probe measurements in MPDX. The two hemispheres are clearly rotating in opposite directions, with the edge momentum transported inward at rates predicted by classical viscous diffusion. At this moderate ionization fraction of $\sim 60\%$ the neutral drag is a significant factor in the momentum transport equation, limiting toroidal flow penetration and forcing flow below measurable levels by $r = 90\,\mathrm{cm}$. In contrast to the large toroidal flows, poloidal velocity flows are too slow to be resolved above the $\sim 1\,\mathrm{km/s}$ probe error; this matches the simulated v_θ values which are less than 500 m/s throughout the spherical volume.

B. Co-rotating hemispheres

A second stirring geometry was tested in MPDX in which all cathodes were installed so as to drive flow in the same (toroidal) direction. This co-rotating flow is designed to be a simple model of the differential flow observed in the solar convective zone, where the equatorial period of 25 days is much shorter than the polar period of 34 days[22]. For this experiment, ten cathodes were distributed between the north and south poles and retracted into the cusp field to $130 < r < 135\,\mathrm{cm}$. Unlike the counter-rotating flow experiment, there is no velocity null between the two hemispheres and so stirring cathodes can be placed at the equator as well as at mid-to-high latitudes. Five velocity probes were scanned, with four of them located in the same magnet ring as a stirring cathode.

Fig.3 shows the results of the co-rotating experiment and their comparison to the hydrodynamic model results. While these helium plasmas had a smaller ionization fraction in comparison to the counter-rotating experiment, the depressed values of the core electron density and neutral fill pressure resulted in lowered dimensionless parameters of $Re = 67$ and $\chi = 11$. However, the magnetic Reynolds number was still quite high at $Rm = 215$ due to comparable measurements of T_e and maximum velocity. The Langmuir probe radial profiles in Fig.3b once again indicate a homogeneous core, albeit with a slight increase in electron temperature and density at the radial position of the LaB_6 cathodes. This local increase is frequently observed in magnet rings with retracted stirring cathodes and is presumably present in the counter-rotating experiment as well. It is more evident here only due to the increased number of probes in cathode rings. Thus, the inputs to the hydrodynamic simulations for both edge-drive experiments were calculated using $R = 130\,\mathrm{cm}$, taking into account the observation that the core volume of homogeneous viscosity and Re extends out only as far as the volume of constant n_e.

The measured velocity profiles in Fig.3d show a uniform rotation direction with relatively small gradients and a non-zero flow in the plasma core. This is partially attributable to the lack of a velocity null near the equatorial plane, which in the counter-rotating case served to further suppress flow far from the vessel wall. In addition, the smaller values of Re and χ here increased radial momentum flux and decreased the loss of momentum to charge-exchange collisions. A downside to decreased Re is decreased poloidal flow, and the modeled flows agree with probe measurements of v_θ insofar as both are below the Mach probe noise level. The measured velocity gradients are a poorer match to simulation results, at least at radial positions closer to the edge cusp field; this may be due to a lack of spherical symmetry in neutral outgassing or some other transport-induced local change in neutral drag.

IV. VOLUMETRIC-DRIVEN FLOW

The second method of stirring MPDX plasmas is designed to generate flow profiles appropriate for the study of the MRI. In astrophysical accretion disks, the plasma in the disk itself follows a Keplarian angular velocity

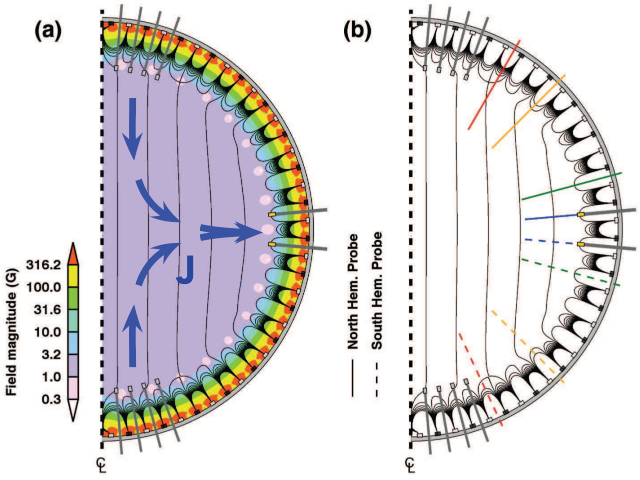

FIG. 4. Experiment setup for volumetric-driven flow: cathodes (gold) are at equator, anodes (grey) are at poles. a) Discharge current is forced across the axial field ($B_z = 2.0\,\mathrm{G}$). b) Scanning probes are distributed across the northern and southern hemispheres.

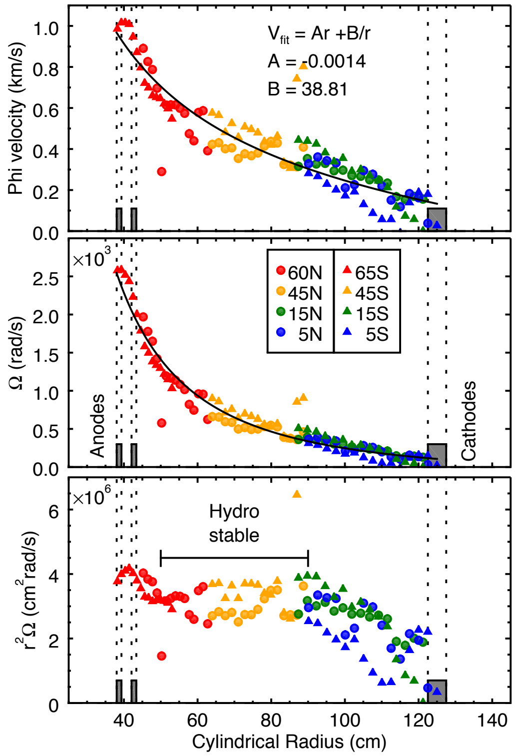

FIG. 5. Velocity probe measurements of toroidal flow in helium plasma.

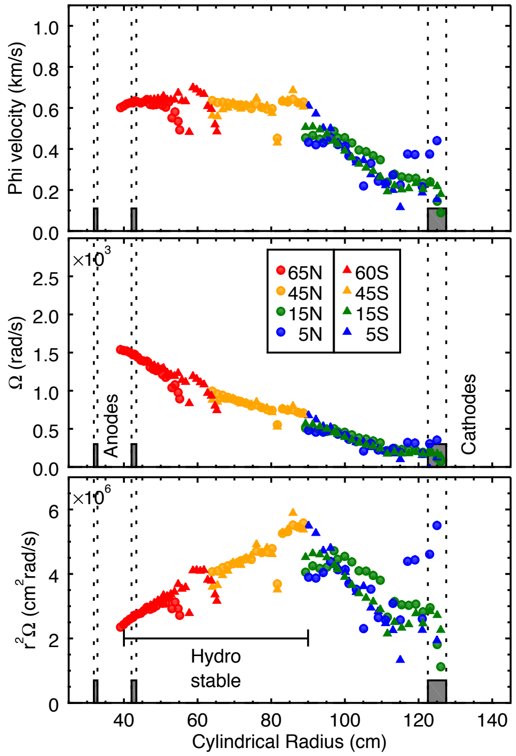

FIG. 6. Velocity probe measurements of toroidal flow in argon plasma.

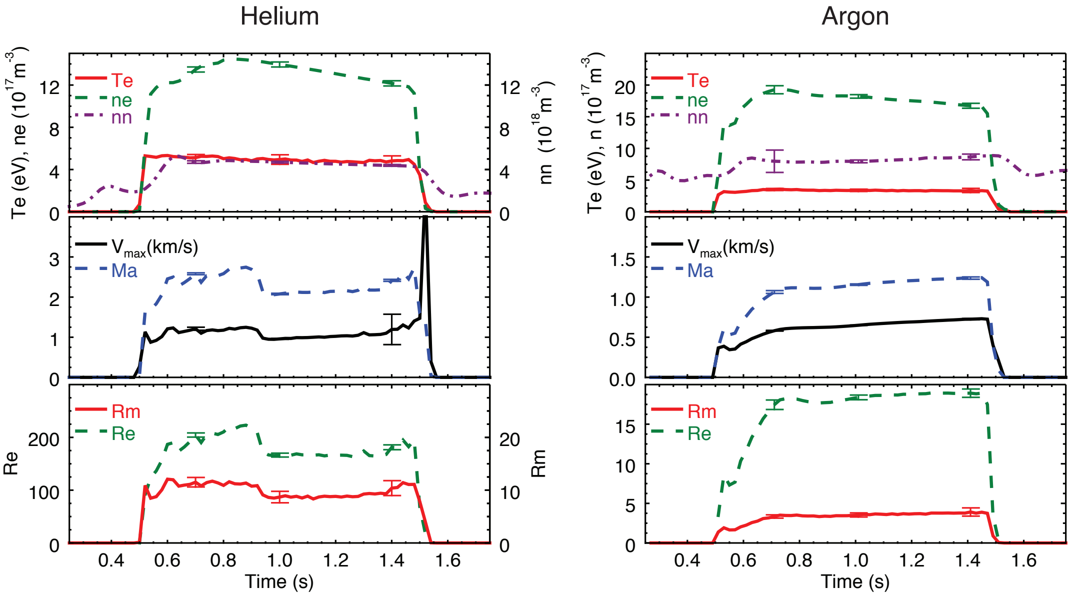

FIG. 7. Global measurements for helium and argon plasma in volumetric flow drive experiments. Fabry-Perot measurements of ion temperature are $T_{i,He} = 0.36\,\mathrm{eV}$ and $T_{i,Ar} = 1.29\,\mathrm{eV}$.

profile[23],

$$\Omega(r) = \sqrt{GM/r^3}. \tag{12}$$

Observations of disk luminosities indicate an accretion rate that far exceeds the expected rate due to classical viscous momentum transport and the MRI acts to facilitate turbulent transport through an MHD instability that arises from the combination of a weak seed magnetic field and shear flow. In order to observe this effect in the laboratory, other sources of plasma turbulence must be avoided while maintaining the correct direction of flow shear. The MRI is destabilized by an angular velocity profile that decreases with radius, while hydrodynamic turbulence is avoided if the angular momentum increases with radius[2],

$$\frac{d\Omega}{dr} < 0, \quad \frac{d(r^2\Omega)}{dr} > 0. \tag{13}$$

where r in this section refers to the cylindrical radius.

This velocity profile is opposite that of the edge-driven flows described in Section III and requires a different flow drive technique. Instead of limiting $\boldsymbol{J} \times \boldsymbol{B}$ torque to the magnetized edge region of MPDX plasmas, a uniform axial magnetic field is externally applied using the 4.07 m diameter Helmholtz coil set. Discharge current that flows in the cylindrical radial direction will generate a $\boldsymbol{J} \times \boldsymbol{B}$ torque throughout the entire volume of the plasma. In order to force current to flow perpendicular to the applied axial field, LaB$_6$ cathodes are installed near the machine equator while anodes are inserted near the north and south poles, as shown in Fig.4. A weak axial field is applied ($B_z = 0.5\,\mathrm{G}$ for helium stirring, $B_z = 2.0\,\mathrm{G}$ for argon stirring) and maintained throughout the duration of the discharge. Current density is larger close to the cylindrical axis of symmetry due to the geometric effects of current continuity and resulting torque profile decreases with cylindrical radius. This flow drive technique produces a velocity profile that has maximum flow near the axis of rotation and slows to a nearly stationary boundary condition at the equatorial plasma edge.

Eight velocity probes were used to measure plasma flow in both hemispheres, in both helium and argon plasmas. Velocity probe measurements are shown in Fig.5 and Fig.6, where data points are identified by probe latitude and hemisphere and correspond to the colored radial chords shown in Fig.4. The probes were distributed so as to completely cover the interval in cylindrical radius spanned by the polar anodes and the equatorial cathodes. It is apparent that the measured flows are symmetric about the vessel equator. This is not a result of well-balanced input current from the anodes; instead, it suggests that *Re* is large enough to for Ferraro's theorem[24] to apply. In this limit of inviscid flow, this predicts that contours of constant magnetic flux are also contours of constant angular velocity. Since the magnetic field is symmetric about the machine equator, this would make the toroidal flow similarly mirrored.

Core measurements for the volumetric flow experiments are shown in Fig.7. The two ion species are an interesting contrast, both in dimensionless parameters and velocity profiles. helium, with a low ion temperature of $T_i = 0.36\,\mathrm{eV}$, has a relatively high *Re* indicating that viscosity is low. The resulting flow is well-fit by Couette flow in a cylinder,

$$v_\phi = Ar + B/r. \tag{14}$$

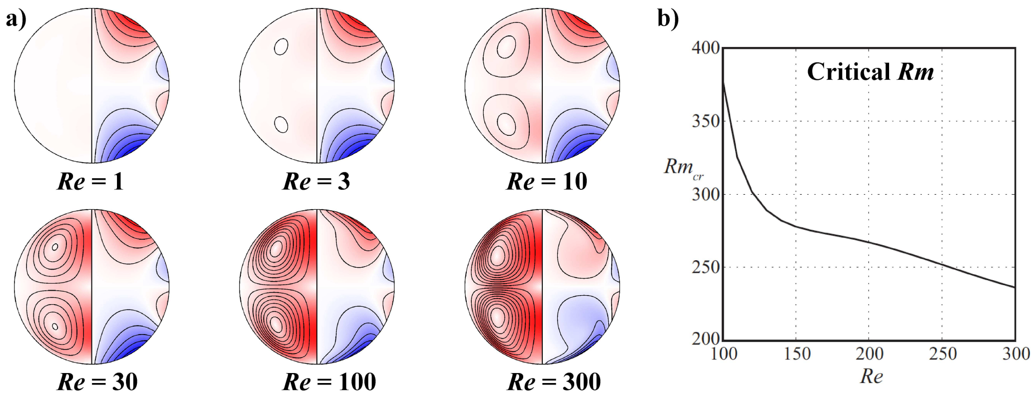

FIG. 8. Optimized counter-rotating flow for $N = 4$ poloidal terms in the edge boundary drive. a) Hydrodynamic model with varying *Re* and zero neutral drag. Scaling and layout are the same as in Fig.2c. b) Critical magnetic Reynolds number for kinematic dynamo excitation as a function of *Re*. Optimized terms and *Re*-*Rm* plot (b) from Khalzov *et al.*[16].

The inner region is marginally stable to the hydrodynamic instability but the radial gradient in angular momentum becomes negative otuside of $r \sim 90\,\mathrm{cm}$. This indicates that the MRI my be active in the inner core of the rotating plasma column and could even be modifying the equilibrium velocity profile to push the outer core into a hydrodynamically unstable regime. A dearth of modeling on this flow drive geometry limits the physical intuition that can be applied to these measurements, but in general the data shows promise for future MRI studies in helium plasmas. The Alfvén Mach number Ma is consistently larger than unity and *Re* is large, indicating that the axial field is weak compared to the generated flows and that viscosity is negligible. Both of these conditions are requirements for the measurement of an MRI mode that is strong enough to overcome both viscous damping and Lorentz force saturation.

In contrast, the argon measurements have a much smaller *Re* due in part to the higher ion temperature of $T_i = 1.29\,\mathrm{eV}$. This plasma flow is more viscous and so momentum diffusion plays a larger role in limiting velocity gradients. The measurements show a flat velocity profile out to $r = 90\,\mathrm{cm}$, which is not well-fit by a Couette-driven flow profile. The inner flow is linearly stable to hydrodynamic instability, but the outer core of the rotating plasma column should undergo a transition to non-axisymmetric modes due to the Rayleigh criterion.

It should be emphasized that no velocity fluctuations have been measured over the course of all MPDX flow experiments. The lack of fluid instability signatures in the Mach probe data points to the possible role of neutrals and viscosity in damping fluid turbulence. In the case of the volumetric helium flow there is minimal neutral burnout in the plasma core, leading to significant neutral drag on the flowing ions. The momentum source term corresponding to the global $\boldsymbol{J} \times \boldsymbol{B}$ torque is large compared to the neutral drag, but smaller-scale turbulent fluctuations could be more susceptible to damping. A similar argument can be applied to the volumetric argon flow which, while being highly ionized, has a small $Re \sim 18$. The larger viscosity could serve to increase the threshold angular momentum gradient for the transition to hydrodynamic turbulence, permitting the observed profiles to exist in a laminar state.

V. CONCLUSIONS

A novel multi-cusp plasma device was built to investigate flow-driven MHD instabilities, and initial experiments have been successful at generating high *Rm* plasma flows. Plasma ionization fractions are in excess of 50% in both helium and argon discharges due in part to the improved confinement afforded by the axisymmetric multicusp geometry. The recent innovations both in permanent magnet energy density and $\mathrm{LaB_6}$ cathode fabrication allow MPDX plasmas to occupy new regions in the *Re*, *Rm* parameter space, outperforming previous magnetic bucket devices and for the first time reaching conditions amenable to generation of the dynamo and MRI.

The various flow geometries presented here are designed to investigate the physical processes the underlie astrophysical instabilities. However, the measured flows and dimensionless parameters are not sufficient to match numerical models that predict magnetic mode growth. In all cases, *Rm* is too low in comparison to the neutral drag force. Specifically, the hydrodynamic flow model results shown in Fig.2 and Fig.3 were used as the equilibrium velocity field in a numerical induction equation solver as described in Khalzov *et al.*[16]. The results are as expected: all magnetic eigenmodes are found to have negative growth rates, and no magnetic amplification is predicted. While optimized flow geometries were found to require *Rm* values between 200 and 300, the measured flow profiles presented here are not identical to the optimized profiles found in Khalzov et al., as shown in Fig.8a. This means that the critical magnetic Reynolds number for the experimental flows is likely to be much larger than the optimized Rm_{crit} shown in Fig.8b. In addition to the non-optimal edge flow drive boundary conditions, the presence of neutral drag also contributes to the discrepancy between measured and optimized flows.

It remains to be seen whether improvements towards an ideal flow structure will produce experimental flows that can generate growing magnetic modes. New plasma heating systems will certainly help, as the current discharge heating scheme makes it difficult to increase *Re* while minimizing χ due their joint dependence on electron density. An electron cyclotron resonant heating (ECRH) system has been installed on MPDX and should permit increases in *Re* and *Rm* as well as the ionization fraction. It is hoped that ERCH will also allow higher electron temperature without a corresponding increase in ion temperature, which also serves to limit *Re*. Future work will take advantage of both this system as well as a significant upgrade in magnetic diagnostics, moving forward towards the experimental detection of these elusive flow-driven MHD instabilities.

ACKNOWLEDGMENTS

This work was funded in part by NSF Award No. PHY 0923258, ARRA MRI, NSF Award No. PHY 0821899, Center for Magnetic Self Organization in Laboratory and Astrophysical Plasmas, and DOE Award No. DE- SC0008709, Experimental Studies of Plasma Dynamos. V. D. acknowledges support by CNRS PICS contract PlasmaDynamo and by French National Research Agency under contract ANR-13-JS04-0003-01. This work was performed under the auspices of the U.S. Department of Energy by Lawrence Livermore National Laboratory under Contract DE-AC52-07NA27344.

IM #LLNL-JRNL-753144

Appendix: 2D Hydrodynamic model

Numerical modeling of axisymmetric flows in the MPDX spherical geometry is a valuable tool in analyzing experimental results. Previous work has established a two-dimensional quasi-spectral code that solves the Navier-Stokes equation (Eq.4) using the boundary condition $\mathbf{v}(R) = v_\phi(\theta)$ at the plasma edge, which is expressed as a sum of spherical harmonics,

$$v_\phi = -\sum_{l=1}^{L} \frac{\tau_l(r)}{r} \frac{\partial P_l(\cos\theta)}{\partial\theta}. \tag{A.1}$$

The discrete polar locations of the stirring cathodes are decomposed into Fourier harmonics,

$$v_\phi = \sum_{n=1}^{N} a_n \sin 2n\theta + b_n \cos 2n\theta, \tag{A.2}$$

which are integrated to give the spherical harmonic coefficients τ_l that are the main input into the hydrodynamic Navier-Stokes solver,

$$\tau_l = \sum_{n=1}^{N} (F_{ln} a_n + G_{ln} b_n), \tag{A.3}$$

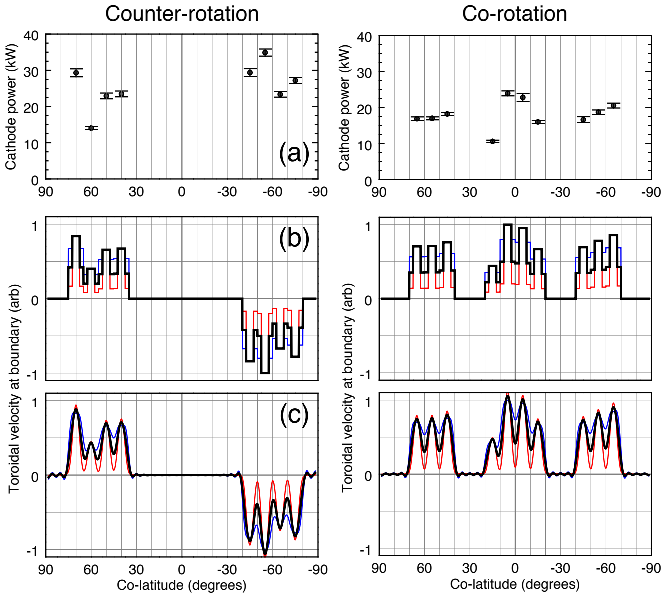

FIG. 9. a) Measured discharge power for each cathode as a function of machine latitude. b) Discretized boundary drive v_ϕ with three possible scalings of flow between cathode rings: red=0.2, black=0.5, blue=0.8. c) Smoothed form of discretized boundary drive using $L = 72$ spherical harmonics.

where the coefficients F_{ln} and G_{ln} are the integrals,

$$F_{ln} = \frac{2l+1}{2l(l+1)} \int_0^\pi \sin 2n\theta \sin^2\theta \frac{\partial P_l(\cos\theta)}{\partial\theta} d\theta, \tag{A.4}$$

$$G_{ln} = \frac{2l+1}{2l(l+1)} \int_0^\pi \cos 2n\theta \sin^2\theta \frac{\partial P_l(\cos\theta)}{\partial\theta} d\theta. \tag{A.5}$$

Fig.9 shows the discrete and spherical harmonic forms of the edge boundary conditions used for the counter- and co-rotation models discussed above. Also shown are the measured cathode discharge powers used to scale the edge boundary conditions. The red and blue curves indicate edge profiles where the flow between cathode rings has been scaled by 0.8 and 0.2 of the cathode drive amplitude, respectively. The black curve is the 0.5 scaling used in the models shown in Fig.2 and Fig.3.

The axisymmetric hydrodynamic equilibrium is computed using the technique outlined in Khalzov *et al.*[16]. The spherical harmonic expansions of the equilibrium velocity components v_r, v_θ, and v_ϕ are truncated at $L = 72$ to reflect the 36-pole geometry of the multi-cusp edge field, and a uniform radial grid with $N_r = 50$ intervals is used to discretize and solve the dimensionless Navier-Stokes equation. The remaining two equilibrium velocity components are defined as,

$$v_r = \sum_{l=1}^{L} \frac{l(l+1)s_l(r)P_l(\cos\theta)}{r^2}, \tag{A.6}$$

$$v_\theta = \sum_{l=1}^{L} \frac{1}{r}\frac{\partial s_l(r)}{\partial r}\frac{\partial P_l(\cos\theta)}{\partial\theta}, \tag{A.7}$$

where $s_l(r)$ is the radial function for the corresponding poloidal mode expansions.

[1] Z. Stelzer, S. Miralles, D. Cébron, J. Noir, S. Vantieghem, and A. Jackson, Physics of Fluids **27**, 0 (2015).

[2] G. I. Taylor, Philosophical Transactions of the Royal Society A: Mathematical, Physical and Engineering Sciences **223**, 289 (1923).

[3] H. K. Moffatt, Nature **341**, 285 (1989).

[4] S. Chandrasekhar, Proceedings of the National Academy of Sciences **46**, 253 (1960).

[5] P. H. Roberts, Philosophical Transactions of the Royal Society A: Mathematical, Physical and Engineering Sciences **272**, 663 (1972).

[6] D. J. Galloway and M. R. E. Proctor, Nature **356**, 691 (1992).

[7] S. A. Balbus and J. F. Hawley, The Astrophysical Journal **376**, 214 (1991).

[8] Ji, Goodman, and Kageyama, Monthly Notices of the Royal Astronomical Society **325**, L1 (2001).

[9] A. Gailitis, O. Lielausis, S. Dement'ev, E. Platacis, A. Cifersons, G. Gerbeth, T. Gundrum, F. Stefani, M. Christen, H. Hänel, and G. Will, Physical Review Letters **84**, 4365 (2000).

[10] R. Stieglitz and U. Müller, Physics of Fluids **13**, 561 (2001).

[11] M. D. Nornberg, E. J. Spence, R. D. Kendrick, C. M. Jacobson, and C. B. Forest, Physics of Plasmas **13**, 055901 (2006).

[12] R. Monchaux, M. Berhanu, M. Bourgoin, M. Moulin, P. Odier, J.-F. Pinton, R. Volk, S. Fauve, N. Mordant, F. Pétrélis, A. Chiffaudel, F. Daviaud, B. Dubrulle, C. Gasquet, L. Marié, and F. Ravelet, Physical Review Letters **98**, 044502 (2007).

[13] E. Schartman, H. Ji, and M. J. Burin, Rev. Sci. Instrum. **80**, 024501 (2009).

[14] C. Collins, M. Clark, C. M. Cooper, K. Flanagan, I. V. Khalzov, M. D. Nornberg, B. Seidlitz, J. Wallace, and C. B. Forest, Physics of Plasmas **21**, 042117 (2014).

[15] I. V. Khalzov, B. P. Brown, F. Ebrahimi, D. D. Schnack, and C. B. Forest, Physics of Plasmas **18**, 032110 (2011), arXiv:1103.5041.

[16] I. V. Khalzov, B. P. Brown, C. M. Cooper, D. B. Weisberg, and C. B. Forest, Physics of Plasmas **19**, 112106 (2012).

[17] F. Ebrahimi, S. C. Prager, and D. D. Schnack, The Astrophysical Journal **698**, 233 (2009).

[18] C. M. Cooper, J. Wallace, M. Brookhart, M. Clark, C. Collins, W. X. Ding, K. Flanagan, I. Khalzov, Y. Li, J. Milhone, M. Nornberg, P. Nonn, D. Weisberg, D. G. Whyte, E. Zweibel, and C. B. Forest, Physics of Plasmas **21**, 013505 (2014).

[19] S. Braginskii, Reviews of Plasma Physics **1**, 205 (1965).

[20] C. M. Cooper, D. B. Weisberg, I. Khalzov, J. Milhone, K. Flanagan, E. Peterson, C. Wahl, and C. B. Forest, Physics of Plasmas **23**, 102505 (2016).

[21] E. Bullard and H. Gellman, Philosophical Transactions of the Royal Society A: Mathematical, Physical a

[22] M. S. Miesch and J. Toomre, Annual Review of Fluid Mechanics **41**, 317 (2009).

[23] S. A. Balbus, Annual Review of Astronomy and Astrophysics **41**, 555 (2003).

[24] V. C. A. Ferraro, Monthly Notices of the Royal Astronomical Society **97**, 458 arXiv:arXiv:1011.1669v3.